

Article

Real-Time Wavelet-Based Coordinated Control of Hybrid Energy Storage Systems for Denoising and Flattening Wind Power Output

Tran Thai Trung ¹, Seon-Ju Ahn ^{1,*}, Joon-Ho Choi ¹, Seok-II Go ¹ and Soon-Ryul Nam ²

¹ Department of Electrical Engineering, Chonnam National University, Gwangju 500-757, Korea; E-Mails: trantrung1811@gmail.com (T.T.T.); joono@chonnam.ac.kr (J.-H.C.); riseisgood@nate.com (S.-I.G.)

² Department of Electrical Engineering, Myongji University, Yongin 449-728, Korea; E-Mail: ptsouth@mju.ac.kr

* Author to whom correspondence should be addressed; E-Mail: sjahn@jnu.ac.kr; Tel.: +82-62-530-1738; Fax: +82-62-530-1749.

External Editor: Frede Blaabjerg

Received: 30 July 2014; in revised form: 25 September 2014 / Accepted: 9 October 2014 / Published: 16 October 2014

Abstract: Since the penetration level of wind energy is continuously increasing, the negative impact caused by the fluctuation of wind power output needs to be carefully managed. This paper proposes a novel real-time coordinated control algorithm based on a wavelet transform to mitigate both short-term and long-term fluctuations by using a hybrid energy storage system (HESS). The short-term fluctuation is eliminated by using an electric double-layer capacitor (EDLC), while the wind-HESS system output is kept constant during each 10-min period by a Ni-MH battery (NB). State-of-charge (SOC) control strategies for both EDLC and NB are proposed to maintain the SOC level of storage within safe operating limits. A ramp rate limitation (RRL) requirement is also considered in the proposed algorithm. The effectiveness of the proposed algorithm has been tested by using real time simulation. The simulation model of the wind-HESS system is developed in the real-time digital simulator (RTDS)/RSCAD environment. The proposed algorithm is also implemented as a user defined model of the RSCAD. The simulation results demonstrate that the HESS with the proposed control algorithm can indeed assist in dealing with the variation of wind power generation. Moreover, the proposed method

shows better performance in smoothing out the fluctuation and managing the *SOC* of battery and EDLC than the simple moving average (SMA) based method.

Keywords: wind generation; electrical energy storage system (EESS); real-time wavelet transform; energy management; fluctuation mitigation; real time digital simulation; Ni-MH battery (NB); electric double-layer capacitor (EDLC)

1. Introduction

Recently, the exhaustion of fossil fuels and the critical environmental pollution have led to the need to develop new clean energy sources. Wind energy, a type of renewable and environmental-friendly energy, is considered as a prospective replacement for conventional energy resources. However, because of the stochastic and intermittent characteristic of wind speed, the resulting fluctuation in power output is the greatest obstacle to the increasing penetration level of wind power in power grids [1]. In order to reduce the negative impact of these fluctuations on the stability, reliability and protection of the power system, a number of control methods have been proposed.

Many researchers have demonstrated that pitch angle control, in conjunction with other modern controllers such as the fuzzy logic controller, provides a very effective means of regulating aerodynamics to reduce wind power fluctuation [2]. However, the short-term fluctuations of wind power output cannot be mitigated by these types of controllers because of the mechanical stress accrued by the wind blade. Abedini *et al.* [3] used a rotor inertia adjustment method to smooth out wind power output. This approach also does not require any energy storage devices but the rotor speed no longer can be controlled to follow maximum power tracking.

An electrical energy storage system (EESS) is recognized as an alternative technique to mitigate both short-term and long-term wind power fluctuations. Various benefits of using EESS in wind power applications are discussed in [4]. The cooperation of different storage devices with different charge/discharge characteristics makes it possible to balance both power- and energy-scale requirements. Among various hybrid energy storage system (HESS) options, this paper focuses on the Ni-MH battery (NB)-electric double-layer capacitor (EDLC) HESS as a solution to mitigate the wind power fluctuation. EDLC is suitable for denoising wind power output because it has a number of exceptional characteristics, including high power density, fast charge/discharge process, high efficiency, and long lifetime [5]. On the other hand, NB with high energy density characteristic is fit for flattening wind power fluctuations.

In the existing literature, a moving average technique and the first-order delay filter (FDF), the simplest methods, have been applied to smooth out wind power fluctuation [6–10]. Ushiwata *et al.* [6] presented a smoothing approach to mitigate wind power fluctuations using EDLC and the simple moving average (SMA) control method. Tanabe *et al.* [7] used FDF with an adjustable time constant and additional rate limiter to keep the fluctuation of wind power output within 10% for 20 min, while Sheikh *et al.* [8] proposed a hybrid control algorithm including both SMA and exponential moving average (EMA) to generate output power reference of static synchronous compensator (STATCOM)/superconducting magnetic energy storage (SMES) system. A state-of-charge (*SOC*)

regulation method of a battery in a hybrid wind power/battery energy storage system has been proposed in [9], and hardware-in-the-loop (HIL) simulation studies of a wind turbine coupled with battery supercapacitor EESS has been presented in [10]. Both are based on simple filtering algorithms.

Some researchers have proposed intelligent approaches for EESS power dispatching and scheduling. Suvire *et al.* [11] utilized a fuzzy inference system to control the active power of the distribution static synchronous compensator (DSTATCOM) coupled with flywheel energy storage system to smooth out wind power fluctuation, whereas Mishra *et al.* [12] used a bacteria foraging technique to integrate wind turbine and batteries to maintain a constant grid power output. Li *et al.* [13] proposed a control algorithm cooperating wavelet transform with fuzzy logic control to smooth a hybrid system including photovoltaic and wind power systems by using a battery energy storage system. However, these methods are implemented via non-real time process, which limits the real-time application. Furthermore, they failed to neither ensure the system power output always satisfies ramp rate requirements nor consider to safe working limits of EESS. Jiang *et al.* [14] implemented a wavelet-based capacity configuration and coordinated control algorithm for reducing output power fluctuations of a wind system using a lithium-ion battery-ultra-capacitor energy storage system. Although this paper proposed a novel approach for solving most of the above problems, it still used two stages of wavelet filtering that increase the computational complexity and require wind data prediction algorithm. The various features of the previous researches are summarized in Table 1.

Table 1. Comparison of various wind power smoothing methods. *SOC*: state-of-charge; *SMA*: simple moving average; *EDLC*: electric double-layer capacitor; *EMA*: exponential moving average; and *SMES*: superconducting magnetic energy storage.

Literature	Filtering method	Storage type	<i>SOC</i> regulation	Interconnection requirement	Real-time or hardware test
Ushiwata [6]	SMA	EDLC	X	X	X
Tanabe [7]	SMA	Battery	X	O	X
Sheikh [8]	SMA + EMA	SMES	X	X	X
Yoshimoto [9]	First order lag filter	Battery	O	X	X
Li [10]	SMA	Battery/EDLC	X	X	O
Suvire [11]	Fuzzy logic + SMA	Flywheel	X	X	X
Mishra [12]	Bacteria foraging	Battery	X	X	X
Li [13]	Fuzzy logic + wavelet	Battery	O	X	X
Jiang [14]	Online wavelet	Battery/EDLC	O	O	X
Proposed	Online wavelet	Battery/EDLC	O	O	O

From the above literature review, the requirements of the wind HESS system can be summarized as follows: (i) better performance in smoothing out the wind power fluctuation; (ii) efficient energy management of HESS for *SOC* regulation; (iii) grid interconnection requirement; and (iv) easy implementation in actual hardware. Considering the above requirements, this paper proposes a novel real-time wavelet-based energy management algorithm (RWEMA) to coordinate a NB-EDLC HESS. The proposed algorithm includes the *SOC* regulation strategies considering practical issues, such as charge/discharge losses and inverter efficiency. For improved filtering and the real-time applicability, we adopted the online wavelet transform proposed in [15]. The real-time digital simulator (RTDS),

which provides reliable and accurate computation in hard real time, is used to model the system and to implement and validate the proposed algorithm [16].

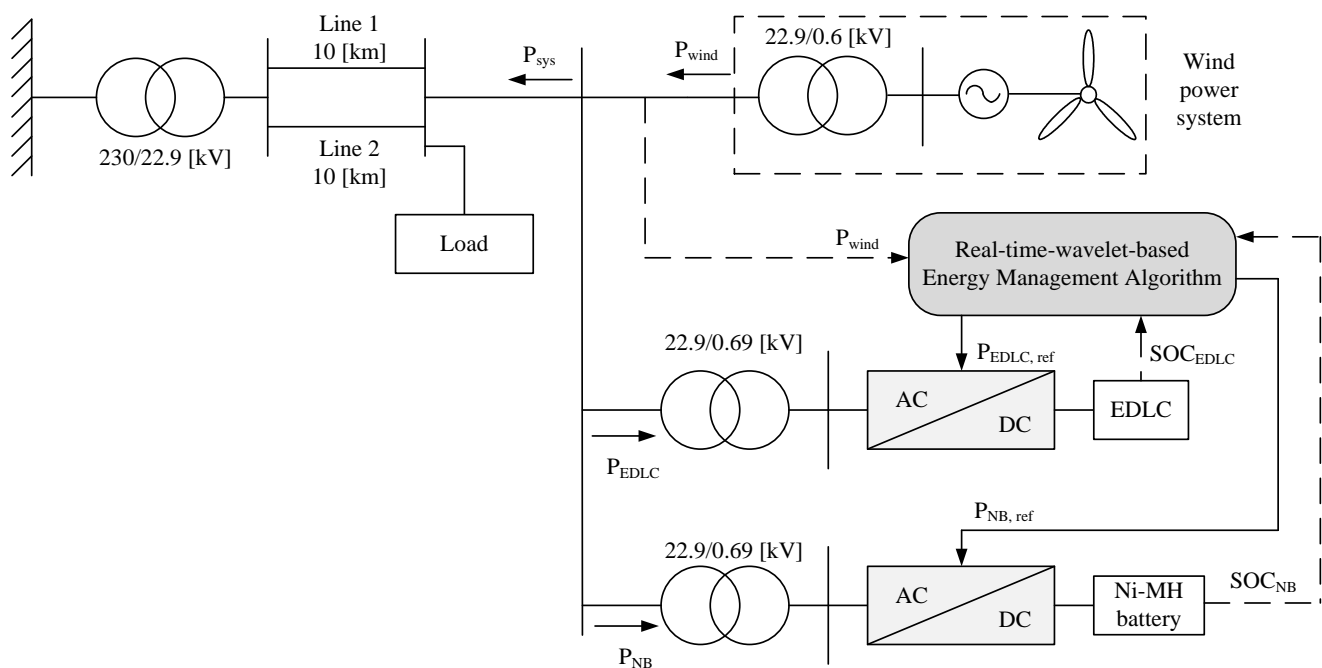
This paper is organized as follows: Section 2 presents the modeling of each energy storage device; Section 3 introduces the RWEMA; in Section 4, the simulation studies are carried out in the RTDS/RSCAD environment to validate the effectiveness of the proposed algorithm; finally, some conclusions are given in Section 5.

2. Wind-Hybrid Energy Storage System Modeling in RSCAD

Integrating EESS with a wind power system will reduce the power output fluctuation. In order to reduce both short-term and long-term fluctuations, this paper proposes the combination of the NB and EDLC energy storage system to satisfy both high power and energy capacity requirements.

The typical wind power system as illustrated in Figure 1 is used for simulation studies in this research. In this system, an induction machine-based wind turbine is integrated with the corresponding HESS. A Vestas V82 wind turbine model is provided in the RSCAD library (Winnipeg, MB, Canada), but the simulation models of the NB and EDLC are not given in the RSCAD. Therefore, the RSCAD simulation models of NB and EDLC are developed based on general mathematical models.

Figure 1. Wind-hybrid energy storage system (HESS) model.



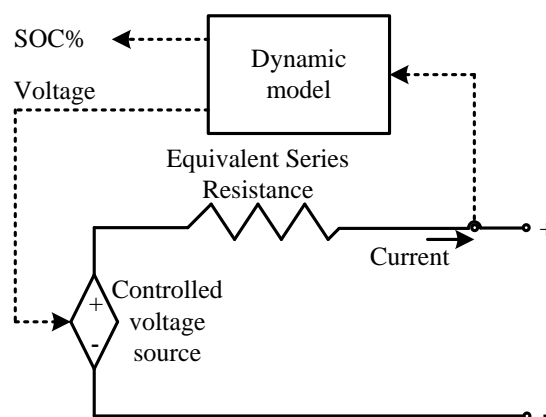
A RWEMA is added to provide the charge/discharge references $P_{EDLC,ref}$ and $P_{NB,ref}$, which are then fed to the corresponding DC/AC inverter. The total active power at the point of common coupling (PCC) P_{sys} is the sum of the wind power output, EDLC, and the NB output (P_{wind} , P_{EDLC} , and P_{batt} , respectively).

2.1. Development of Electric Double-Layer Capacitor Simulation Model in RSCAD

EDLC is an electrochemical capacitor that consists of two electrodes to allow a potential to be applied across the cell; two double layers are therefore present, one at each electrode/electrolyte interface.

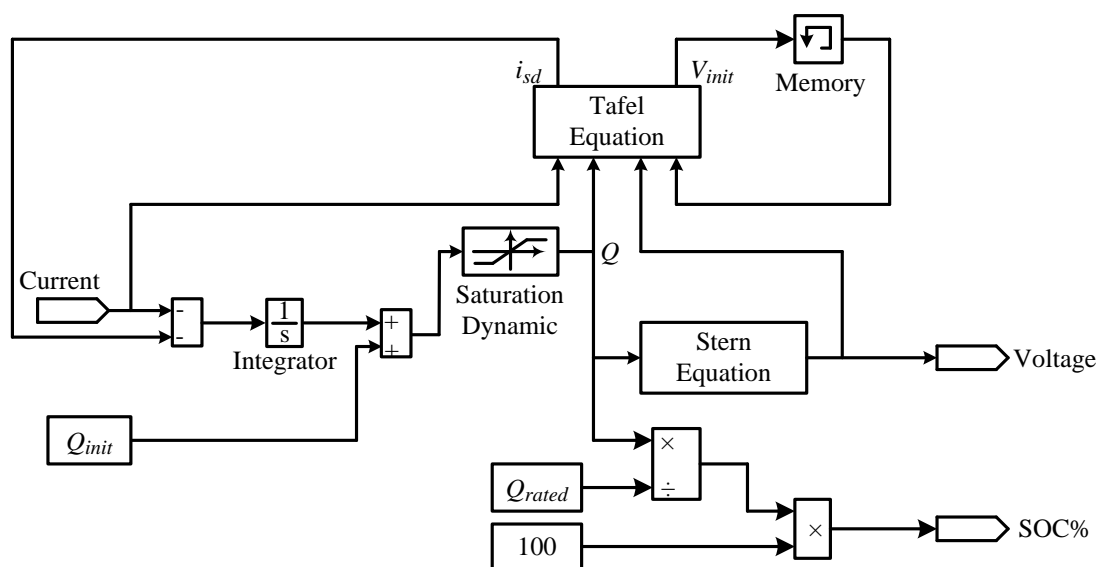
Since EDLC has a number of advantages such as high power density, fast charge/discharge process, long lifetime and low temperature performance, it is considered to be a very promising energy storage device used to mitigate short-term fluctuation of wind power output [17]. For the simulation studies, EDLC is modeled as an ideal voltage source in series with an equivalent resistance, where the value of the voltage source is calculated from the dynamic model, as shown in Figure 2.

Figure 2. Equivalent circuit of EDLC simulation model in RSCAD.



The dynamic model represents the electrochemical behavior of EDLC. In this paper, a mathematical model consisting of Stern and Tafel equations is used that gives the relationship between voltage, current and the available amount of charge during charging/discharging processes [18]. The input of this model is the current obtained from the terminal of EDLC, and the outputs are the voltage and the SOC of EDLC. The detailed block diagram of the dynamic model is shown in Figure 3.

Figure 3. Block diagram of the detailed dynamic model.



The amount of electric charge in EDLC (Q) is calculated as Equation (1), where Q_{init} is the initial amount of charge, i is the measured current, and i_{sd} is the self-discharge current:

$$Q = Q_{init} + \int_0^t -(i(\tau) + i_{sd}(\tau)) d\tau \quad (1)$$

The saturation limit function is used to restrict the calculated amount of charge within a specific range to prevent the full discharge and overcharge of EDLC. The Tafel equation given by Equation (2) is used to calculate the leakage current i_{sd} that represents the self-discharge phenomenon of EDLC:

$$i_{sd}(t) = -S \cdot i_0 \cdot N_c \cdot \exp \left\{ \frac{\alpha \cdot F}{R \cdot T} \cdot \left(\frac{V}{N_s} - \frac{V_{max}}{N_s} - \Delta V \right) \right\} \quad (2)$$

Finally, the voltage value of the controlled voltage source is obtained from the Stern equation as follows:

$$V = \frac{N_c \cdot N_s \cdot Q \cdot r}{N_p \cdot N_c^2 \cdot \epsilon \cdot S} + \frac{N_c \cdot N_s \cdot 2 \cdot R \cdot T}{F} \cdot \alpha \cdot r \cdot \sinh \left(\frac{Q}{N_p \cdot N_c^2 \cdot S \sqrt{8 \cdot R \cdot T \cdot \epsilon \cdot c}} \right) \quad (3)$$

where:

- N_c number of layers of electrodes;
- N_s number of series EDLC cells;
- N_p number of parallel EDLC cells;
- Q electric charge (C);
- r molecular radius (m);
- ϵ permittivity of material;
- S interfacial area between electrodes and electrolyte (m²);
- R ideal gas constant;
- T operating temperature (F);
- α charge transfer coefficient;
- c molar concentration (mol m⁻³);
- i_0 exchange current density;
- F faraday constant;
- V_{max} surge voltage (V);
- ΔV over-potential (V).

The additional details of parameter declaration and calculation are given in [19]. The other required parameters are computed from basic electrochemical equations and some known constants such as Avogadro, ideal gas and Stefan-Boltzmann constants, *etc.*

In order to represent different initial *SOC* level of EDLC, the initial amount of charge of EDLC (Q_{init}) should be calculated before the simulation starts. Since the capacitance of EDLC is nonlinear and dependent on the open circuit voltage, Q_{init} can be represented by a function of the initial open circuit voltage (V_{init}), governed by:

$$Q_{init}(V_{init}) = C(V_{init}) \cdot V_{init} \quad (4)$$

For the purpose of simplifying the simulation model, the above nonlinear voltage-capacitance dependence is rewritten so that the capacitance C is kept constant while Q_{init} is approximated as follows:

$$Q_{init}(V_{init}) = C \cdot f(V_{init}) \quad (5)$$

The function $f(V_{init})$ is obtained for a specific EDLC module under test, which consists of 3000 F Maxwell BootsCap Devices (San Diego, CA, USA). For this, the simulation is implemented with an EDLC model provided by Simscape module in MATLAB Simulink [19]. The Q_{init} data is captured by changing the initial voltage from 0 V to 2.8 V (equivalent to SOC level from 0% to 100%) while the EDLC is either fully charged or fully discharged with a constant current. From the simulation data, the relationship between V_{init} and Q_{init} is established by curved fitting as follows:

$$f(V_{init}) = -0.001822 \cdot (V_{init})^6 + 0.018478 \cdot (V_{init})^5 - 0.073154 \cdot (V_{init})^4 + 0.125816 \cdot (V_{init})^3 + 0.012911 \cdot (V_{init})^2 + 0.766703 \cdot (V_{init}) + 0.001655 \quad (6)$$

Based on the above mathematic model, a user-defined model (UDM) of EDLC is made by using the component builder in the RSCAD. From the configuration interface of the developed UDM, the parameters of EDLC can be modified to satisfy the requirements of different simulation cases, as shown in Figure 4.

Figure 4. EDLC model parameter configuration menu.

Supercap.def					
Tafel parameters		Monitoring		Signal Names	
CONFIGURATION			Supercapacitor Parameters		
Name	Description	Value	Unit	Min	Max
C	Rated capacitance	3000	F	0.1	
Vrated	Rated voltage	2.7	V	0	
Vmax	Surge voltage	2.8	V	0	
Ns	Number of series capacitors	1		1	
Np	Number of parallel capacitors	1		1	
Vinit	Initial voltage	2.7	V	0	
Temp	Operating temperature	25	C	0	

2.2. Development of Ni-MH Battery Simulation Model in RSCAD

The first NB was introduced in 1990 by Sanyo Electric Company in Osaka, Japan. This battery type has a number of advantages such as having high energy density and high efficiency, and containing no toxic metals. Since its response is slower than EDLC, it is used to reduce long-term wind power fluctuation.

NB is also modeled as a controllable voltage source, where the value of the voltage source is calculated from the dynamic model. In this study, the modified Shepherd-based mathematic model of NB presented in [20] is used. This model includes an equation to describe the electrochemical behavior of a battery directly in terms of terminal voltage, open circuit voltage, internal resistance, discharge current, and SOC . This model is based on a number of specific assumptions and limitations, including the internal resistance is supposed to be constant and temperature effect is not considered.

The value of the voltage source during the discharge and charge process can be calculated by using Equations (7) and (8), respectively:

$$V_{\text{batt}} = E_0 - R_b \cdot i - K \cdot \frac{Q}{Q - it} \cdot (it + i^*) + \text{Exp}(t) \quad (7)$$

$$V_{\text{batt}} = E_0 - R_b \cdot i - K \frac{Q}{|it| - 0.1 \cdot Q} \cdot i^* - \underbrace{K \frac{Q}{Q - it} \cdot it}_{\text{Pol. Voltage}} + \text{Exp}(t) \quad (8)$$

where:

- V_{batt} battery voltage (V);
- E_0 battery constant voltage (V);
- K polarization constant (V/A h) or polarization resistance (Ω);
- Q battery capacity (A h);
- it actual battery charge (A h);
- A exponential zone amplitude (V);
- B exponential zone time constant inverse (A h)⁻¹;
- R internal resistance (Ω);
- i battery current (A);
- i^* filtered current (A).

Based on Equations (7) and (8), the UDM of NB is also created by using the component builder module in the RSCAD environment. Figure 5 shows the main parameter configuration menu of the NB model. The parameters and stack configuration of the battery can be modified through this interface.

Figure 5. Battery model parameter configuration menu.

Ni-MH battery.def					
CONFIGURATION		Battery parameters	Battery Array	Monitoring	
Name	Description	Value	Unit	Min	Max
E0	Battery Constant voltage	1.26	V		
K	Polarization Constant	0.0001204	V/Ah		
Q	Battery Capacity	105.285	Ah		
A	Exponential Zone Amplitude	0.1154			
B	Exponential Zone Time Constant Inverse	0.1108	Ah-1		
R	Internal Resistance	0.0004576	Ohm		
iVbat	initial battery voltage	1.39	V		

3. Real-Time Wavelet-Based Energy Management Algorithm

The application of discrete wavelet transform (DWT) in the wind power system is actually a filtering process, in which the wind power output is decomposed into smoothed and noised components.

This process can be classified into non-real-time and real-time methods. In this paper, a real-time wavelet method is implemented based on a moving window function (MWF) [15]. This MWF has a length of n and is designed to store wind power output data as a first-in first-out buffer. The proposed RWEMA controller dynamically obtains the results from MWF and the SOC from the EDLC and NB bank, and then determines the reference value for the corresponding DC/AC inverter controller of HESS. Furthermore, the SOC control strategies are added to maintain the SOC levels of storage within their safe operating limits, which are normally between 20% and 80% for battery [14] and between 30% and 90% for EDLC.

The objective of the proposed RWEMA is to both denoise and flatten the total wind-HESS system output during the specified time period. In order to obtain a constant total power output every 10 min, an average buffer with a length of m is used in the RWEMA. The procedure of the proposed RWEMA consists of three key stages: data processing and DWT procedure, SOC control strategy, and ramp rate limitation (RRL).

3.1. Data Processing and Discrete Wavelet Transform Procedure

Step 1: During the first n seconds, the wind power output data is sampled every second and added to the MWF:

$$\{P_w^t | t = 1, 2, \dots, n-1, n\} \quad (9)$$

Step 2: As soon as the MWF is filled, the MWF is extended by using a short-symmetric method to deal with some of the disadvantages of real-time wavelet transform such as border distortion and the pseudo-Gibbs phenomena [15]. The length of MWF is increased, and the pre-processed wind power series becomes:

$$\left\{ P_w^1, P_w^2, \dots, P_w^{n-1}, P_w^n, \underbrace{P_w^n, P_w^{n-1}, \dots, P_w^{n-\Delta t}}_{\text{Short-Symmetric}} \right\} \quad (10)$$

Step 3: The wind power output in the extended MWF is decomposed into two corresponding components by passing it through low-pass and high-pass filter to the l -th level. The level- l low-frequency component and the sum of the l -level high-frequency terms are:

$$\{P_A^t | t = 1, 2, \dots, n-1, n, n, n-1, \dots, n-\Delta t\} \quad (11)$$

$$\{P_D^t | t = 1, 2, \dots, n-1, n, n, n-1, \dots, n-\Delta t\} \quad (12)$$

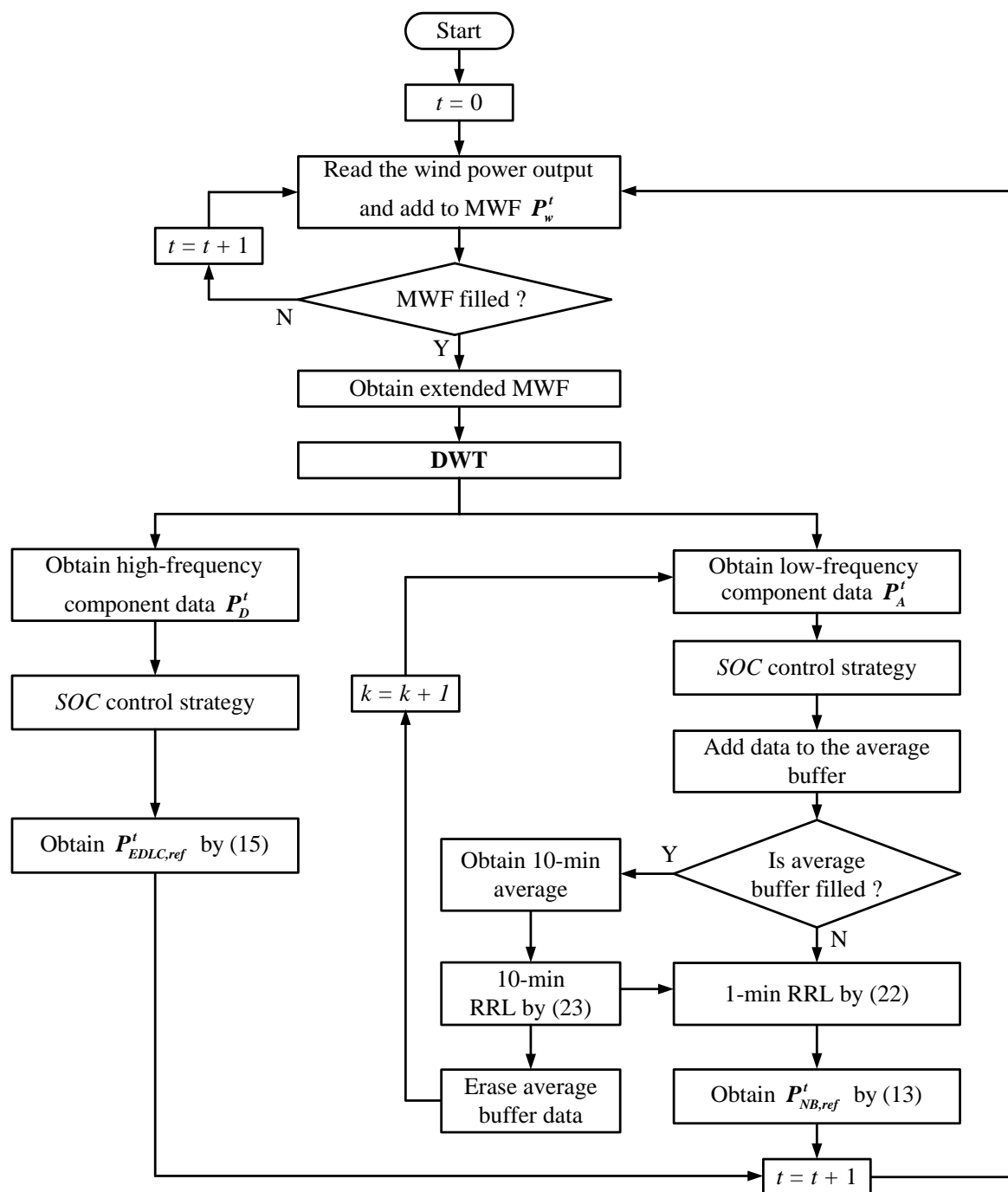
Step 4: The n -th data of the high and low frequency component are sent to SOC control strategy stage described in Section 3.2. The modified high frequency component is directly used to determine the active power reference for the inverter controller of EDLC. The modified low frequency component is then added to the average buffer. As soon as the average buffer is filled, the system output reference for the next 10 min ($P_{\text{sys,ref}}^k$) is calculated by taking the average of the buffer and applying the 10-min RRL constraint given in Section 3.3. The system output reference at time t

($P_{\text{sys,ref}}^t$) is calculated considering the 1-min RRL requirement, and finally the reference for the NB inverter controller is determined by using:

$$P_{\text{NB,ref}}^t = P_A^t - P_{\text{sys,ref}}^t \quad (13)$$

Step 5: Subsequently, the new data from the wind power output is added to the last position of MWF and the first data is removed. Repeat Steps 2–5 with the updated MWF. A flowchart of the complete algorithm is illustrated in Figure 6.

Figure 6. Flowchart of the complete real-time wavelet-based energy management algorithm (RWEMA). MWF: moving window function; DWT: discrete wavelet transform; and RRL: ramp rate limitation.



Since the average of the previous 10-min period is used as a reference for the next period, the proposed method does not require any additional forecasting technique. The combined power output of the wind turbine and HESS defined by Equation (14) is denoised and kept almost constant during the 10 min period:

$$P_{\text{sys}}^t = P_{\text{w}}^t - P_{\text{NB}}^t - P_{\text{EDLC}}^t \quad (14)$$

where:

- P_{sys}^t power output of the wind-HESS system at time t ;
- P_{w}^t power output of the wind turbine at time t ;
- P_{NB}^t power charged into NB at time t ;
- P_{EDLC}^t power charged into EDLC at time t .

3.2. State-of-Charge Control Strategies

The *SOC* levels of the storage devices continuously vary during the charge/discharge process. Furthermore, the non-ideal charging and discharging efficiency of NB and EDLC slowly reduces their *SOC* level. Since the capacity of the storage devices is limited, the *SOCs* of NB and EDLC may exceed their safe operating limits. In that case, HESS will be disconnected from the grid for safety, and the regulation effect will no longer exist. To avoid or even reduce these unexpected situations, this paper proposes *SOC* control strategies.

3.2.1. State-of-Charge Control Strategy of the Electric Double-Layer Capacitor

The high frequency component P_{D}^t is basically used as a reference value for the EDLC inverter controller ($P_{\text{EDLC,ref}}^t$). In order to keep the *SOC* within the specified limits, an offset term is added to P_{D}^t as Equation (15), where α_{EDLC} is a tuning constant determined depending on the EDLC *SOC* level, and $P_{\text{EDLC,rated}}$ is the rated power of the EDLC:

$$P_{\text{EDLC,ref}}^t = P_{\text{D}}^t + \alpha_{\text{EDLC}} \cdot P_{\text{EDLC,rated}} \quad (15)$$

If the *SOC* level is within a safe range, 45%–75% in this research, the offset term will be zero. If the *SOC* level is above this range, the offset term should be negative in order to reduce charging or increase discharging, while the term should be positive in the opposite case. Moreover, the magnitude of the offset term should increase as the *SOC* level further deviates from the safe range.

When the losses during the charge/discharge process are considered, the offset term is slightly modified. Considering the efficiency of the EDLC and the inverter, the charged ($P_{\text{EDLC,c}}$) and discharged ($P_{\text{EDLC,d}}$) power can be calculated as follows:

$$P_{\text{EDLC,c}} = \eta_{\text{c}} \cdot \eta_{\text{inv}} \cdot P_{\text{ref,c}} \quad (16)$$

$$P_{\text{EDLC,d}} = \frac{1}{\eta_{\text{d}}} \cdot \frac{1}{\eta_{\text{inv}}} \cdot P_{\text{ref,d}} \quad (17)$$

where η_c and η_d are the charging and discharging efficiency of EDLC, respectively; η_{inv} is the efficiency of the inverter; and $P_{ref,c}$ and $P_{ref,d}$ are the electrical charge and discharge references of EDLC, respectively. Thus, the *SOC* level of EDLC will gradually decrease with time, even though the average value of the charge and discharge reference value is zero. In this paper, the charging and discharging efficiencies of EDLC are assumed to be 98%, whereas the efficiency of the inverter is chosen to be 97%. The power loss in the charge and discharge process is determined as:

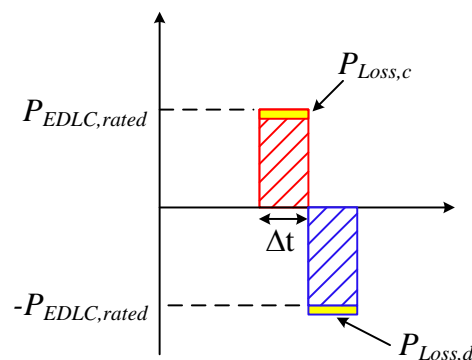
$$P_{Loss,c} = P_{ref,c} - P_{EDLC,c} = (1 - \eta_c \cdot \eta_{inv}) \cdot P_{ref,c} = 0.049 \cdot P_{ref,c} \quad (18)$$

$$P_{Loss,d} = P_{EDLC,d} - P_{ref,d} = \left(\frac{1}{\eta_d} \cdot \frac{1}{\eta_{inv}} - 1 \right) \cdot P_{ref,d} = 0.052 \cdot P_{ref,d} \quad (19)$$

When the electrical charge/discharge value is the rated power of EDLC as shown in Figure 7, the maximum total power loss during a charge/discharge cycle can be expressed as:

$$P_{Loss}^{max} = P_{Loss,c}^{max} + P_{Loss,d}^{max} \approx 0.1 \cdot P_{EDLC,rated} \quad (20)$$

Figure 7. Charge/discharge energy of EDLC with rated power.



The magnitude of the high frequency component of wind power rarely reaches the maximum, and is usually very small compared to the rated power of EDLC. Based on our test, the absolute average of the high frequency component is about 8%–10% of $P_{EDLC,rated}$. Therefore, in this research, the average power loss in EDLC and in the inverter is chosen as 1% of $P_{EDLC,rated}$. To compensate for the loss, this amount of power should be added to the offset term discussed above. The tuning constants for EDLC, considering both the *SOC* level control and loss compensation, are listed in Table 2 according to the *SOC* level.

Table 2. Tuning constant for the *SOC* control of EDLC and Ni-MH battery (NB).

EDLC <i>SOC</i> level	Tuning constant (α_{EDLC})	Battery <i>SOC</i> level	Tuning constant (α_{NB})
$85\% \leq SOC_{EDLC}$	−0.07	$75\% \leq SOC_{NB}$	1.25
$80\% \leq SOC_{EDLC} < 85\%$	−0.03	$70\% \leq SOC_{NB} < 75\%$	1.15
$75\% \leq SOC_{EDLC} < 80\%$	−0.01	$60\% \leq SOC_{NB} < 70\%$	1.05
$45\% \leq SOC_{EDLC} < 75\%$	0.01	$40\% \leq SOC_{NB} < 60\%$	1.0
$40\% \leq SOC_{EDLC} < 45\%$	0.03	$35\% \leq SOC_{NB} < 40\%$	0.85
$35\% \leq SOC_{EDLC} < 40\%$	0.05	$30\% \leq SOC_{NB} < 35\%$	0.75
$SOC_{EDLC} < 35\%$	0.09	$SOC_{NB} < 30\%$	0.65

3.2.2. State-of-Charge Control Strategy of the Ni-MH Battery

The main concept of the *SOC* control strategy for NB is similar to that of EDLC. However, in this case, the NB inverter reference is not directly modified. Instead, the system output reference of the next 10-min period is adjusted according to the change of the NB *SOC* level. If the *SOC* level is above the maximum safe range, the system output reference should be increased so that the discharge power is increased. On the contrary, when the *SOC* level is very low, the *SOC* level can be increased or less reduced by decreasing the system output reference. For this, the low frequency component at time t (P_A^t) is multiplied by a different tuning constant depending on the NB *SOC* level as follows:

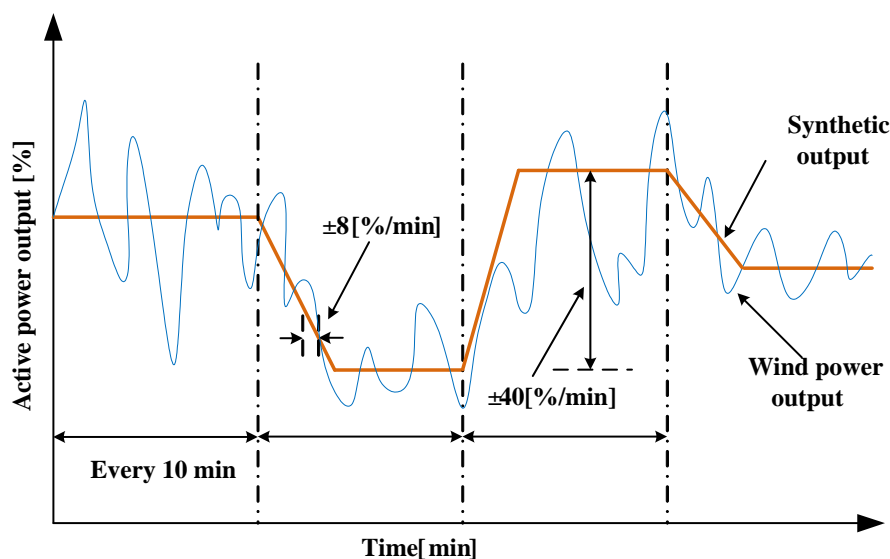
$$P_{A_new}^t = \alpha_{NB} \cdot P_A^t \quad (21)$$

The tuning constant α_{NB} used in the research is summarized in Table 2. It should be noted that the tuning constant for a safe range (40%–60% in this research) is unity, not zero.

3.3. Ramp Rate Limitation Requirement

Since both short-term and long-term wind power fluctuations cause severe negative effects on power system quality, stability, and reliability, they should be restricted within a certain limit, especially at a high wind power penetration level [14]. Several different RRLs have been proposed, depending on the recent situation of wind power of each country or the policies of power utilities. For example, the Hawaiian Electric Company (Honolulu, HI, USA) limits the ramp rate at ± 2 MW/min at all times, whereas in Germany, the maximum ramp rate for a wind power system is 10% of the rated power of the wind turbine ($P_{wt, rated}$) per minute [21]. In this paper, in order to obtain constant total power output every 10 min, two RRLs that were recently used in Ireland are selected, as shown in Figure 8 [22].

Figure 8. 1-min and 10-min RRL requirements.



A 1-min requirement defined by Equation (22) is used to limit the ramp rate of the total power output, while a 10-min requirement in Equation (23) is used to prevent overshooting when the system power

reference is changed. Here, the term k is used to count the change of the system reference every 10 min, whereas the term t represents a 1-s change of system reference:

$$\left| P_{\text{sys, ref}}^t - P_{\text{sys, ref}}^{t-1} \right| \leq \frac{1}{60} \cdot 0.08 \cdot P_{\text{wt, rated}} \quad (22)$$

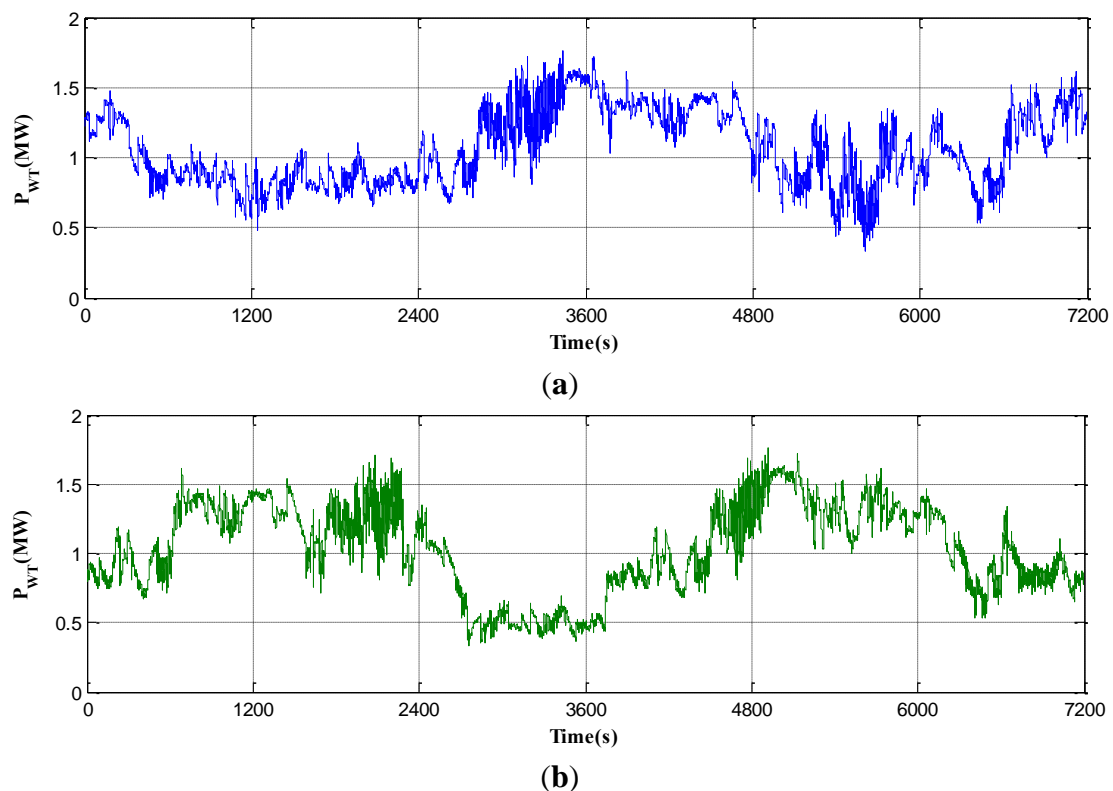
$$\left| P_{\text{sys, ref}}^k - P_{\text{sys, ref}}^{k-1} \right| \leq 0.4 \cdot P_{\text{wt, rated}} \quad (23)$$

4. Simulation Studies

4.1. Configuration of the Test System

The wind-HESS test system shown in Figure 1 is implemented in the RSCAD environment. A Vestas V82 wind turbine model provided in the RSCAD library is used to cooperate with the NB-EDLC HESS. The rated power of the wind turbine is 1.65 MW. Two different wind power output profiles for 2 h (7200 s) shown in Figure 9 are used in the simulations.

Figure 9. Active power output of wind turbine sampled at 1-s resolution: (a) Wind Pattern 1; and (b) Wind Pattern 2.



The capacities of the storage are chosen based on the selected energy management algorithm. The rating of the NB is determined to continuously supply or store 60% of the wind turbine rated power for approximately 600 s. The rating of EDLC is chosen so that it can supply or store 40% of the wind turbine rated power for 60 s. The *SOC* limits and some operational margins are also considered to determine the ratings of the storage. The detail parameters of the test system are summarized in Table 3.

Table 3. Test system parameters.

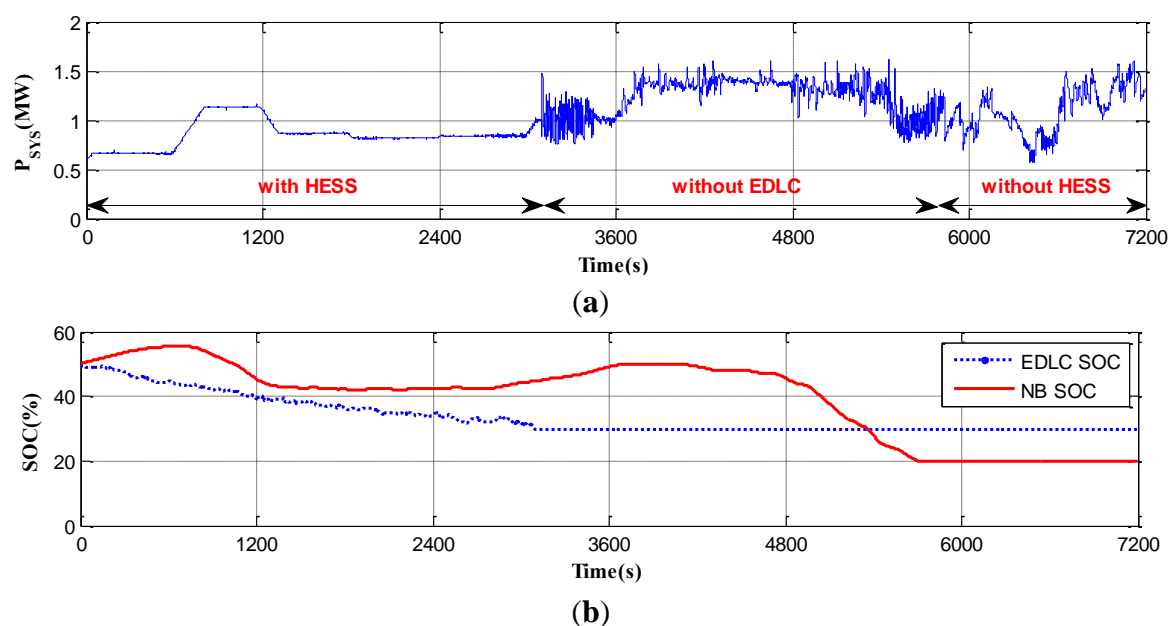
Component	Parameter	Value
Wind turbine	$P_{wt, rated}$	1.65 MW
NB	$P_{NB, rated}$	1.0 MW
	$E_{NB, rated}$	0.305 MW h
EDLC	$P_{EDLC, rated}$	0.66 MW
	$E_{EDLC, rated}$	0.022 MW h

The proposed RWEMA including the DWT algorithm is implemented as a UDM by using the component builder in the RSCAD. In order to satisfy the typical time step (50 μ s) of real-time simulation and to reduce the size of the computation, the length of MWF was selected as $n = 16$. The length of the short-symmetric extension Δt was 4. The decomposition level of DWT was 5, with “Haar” wavelet function [23]. To test the effectiveness of the SOC control strategy, the initial SOC levels of NB and EDLC were set at 50%.

4.2. Case 1: Without State-of-Charge Control Strategy

In this case, we applied the proposed RWEMA without the SOC control strategies; *i.e.*, no adjustment was applied to the EDLC and NB inverter references, regardless of their SOC level. In addition, it is assumed that the NB and EDLC are disconnected if the SOC level is outside the safe operating limits. As shown in Figure 10, the total system power output was successfully denoised and flattened with the help of HESS until the SOC level of EDLC reached its minimum limit (30%) at 3203 s. Subsequently, even though the short-term fluctuation was included in the system output, the average output of the system was more flattened than the original wind power output. After 5706 s, when the SOC level of NB reached its lower limit, the denoising and flattening effects were no longer present and the total power output fluctuation was the same as that of the original wind turbine power output.

Figure 10. Simulation results for Case 1—without SOC control strategy: (a) total system power output; and (b) SOC level of EDLC and NB.



4.3. Case 2: With State-of-Charge Control Strategy and Comparison with Simple Moving Average

In this case, full RWEMA including the SOC control strategy was applied, while the other simulation settings were the same as those for Case 1. The simulation results are represented by blue lines in Figure 11. As shown in Figure 11a, the fluctuation of the wind power output was almost completely eliminated. Moreover, the total power output was kept constant during each 10-min period after the linear ramp up/down in the beginning, which demonstrates that the RRL requirements have been met. The SOC profiles of the NB and EDLC are shown in Figure 11d,e, respectively. It is shown that the SOC of HESS could be adaptively maintained within the safe operating limits with the proposed SOC control strategies.

In addition, we implemented a SMA filtering based method and compared the performance with the proposed wavelet transform based algorithm. The simulation results with SMA are represented by red lines in Figure 11. Although the basic requirements could be achieved with the SMA based method, the short term fluctuation remaining in the system output was larger than the results of the RWEMA case. As shown in Figure 11b,c, the differences in the output of the NB and EDLC between the two methods were not significant. However, the accumulated effects of the differences were reflected in the SOC profiles. For a more detailed comparison, we used several indices as follows:

- (a) Maximum Absolute Value of NB Power Output (P_{NB}^{\max}): since the cost of the inverter is proportional to the power rating, smaller P_{NB}^{\max} implies a lower installation cost.
- (b) Battery health index (BHI): defined in Equation (24), refers to the degree to which the SOC values deviate from the desired level, typically chosen to be 50%. A smaller BHI indicates more effective usage of the storage device within the safe operating limits [14]:

$$BHI = \sqrt{\frac{1}{T} \cdot \sum_{t=1}^T [SOC(t) - 50]^2} \quad (24)$$

- (c) Average power loss of energy storage ($P_{ESS, loss}^{avg}$) and average system output (P_{sys}^{avg}): the losses in the NB and EDLC during the charge/discharge process and the losses in the inverter will affect the total system output. The average system output is closely related to the revenue of the wind power system operator. The average power loss of the NB and EDLC is defined as Equation (25), where $T = 7200$ in this study:

$$P_{ESS, loss}^{avg} = \frac{1}{T} \sum_{t=1}^T P_{ESS}(t) - \frac{SOC(T) - SOC(1)}{100} \cdot \frac{E_{ESS, rated}}{T/3600} \quad (25)$$

Figure 11. Simulation results for Case 2 with Wind Pattern 1: (a) total power output; (b) NB power output; (c) EDLC power output; (d) SOC level of NB; and (e) SOC level of EDLC.

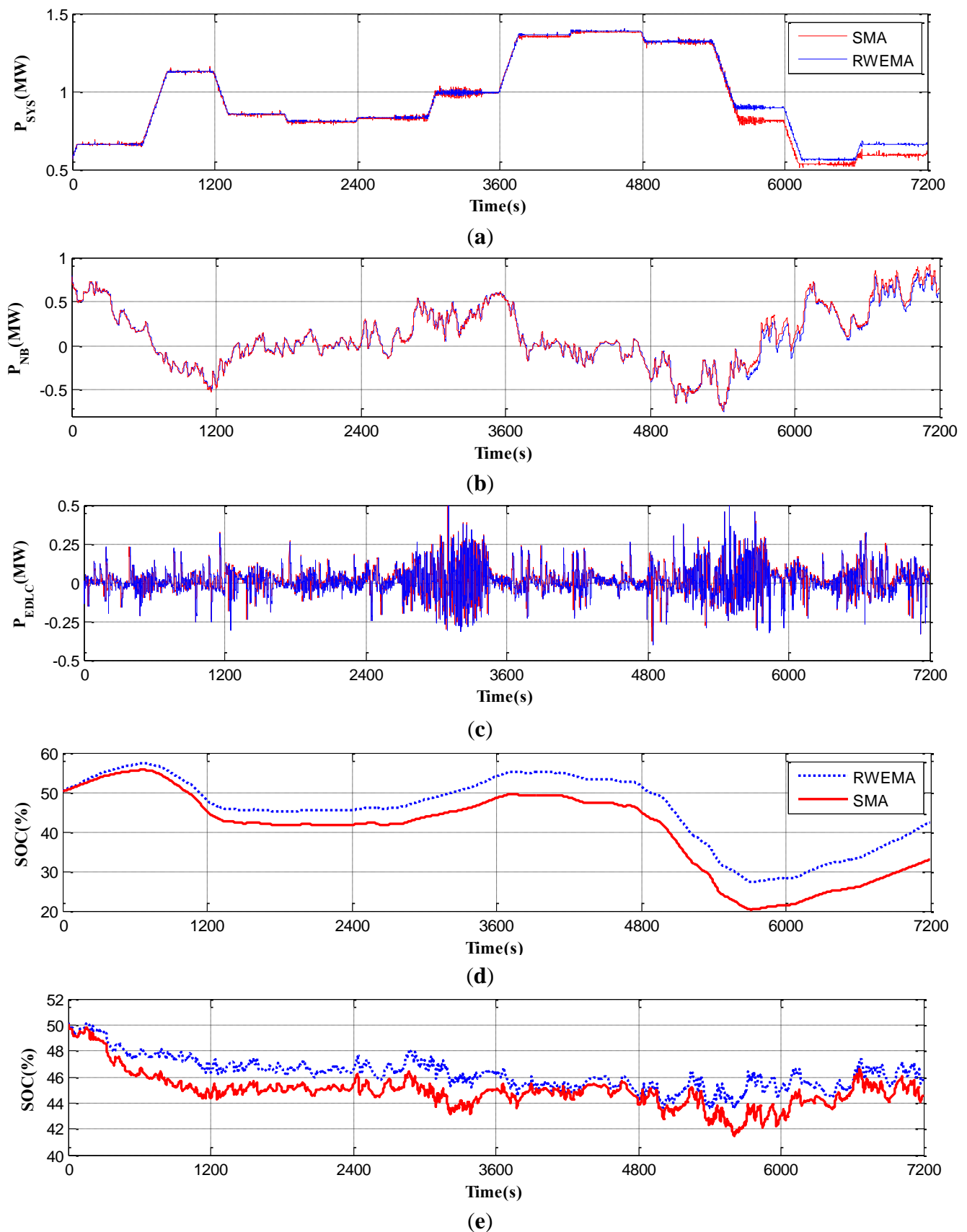


Table 4 summarizes a comparison between the two methods. For the Wind Pattern 1, P_{NB}^{\max} with the RWEMA decreased by 7.79%, and the *BHI* was 29.20% smaller than that of the SMA method. In other words, the proposed RWEMA not only reduces the inverter rating, but also more effectively manages the usage of NB. Moreover, the power losses of NB and EDLC were 18.67% and 40.15% smaller, respectively, than those in the SMA method. Consequently, the total system power output was increased by 0.017 MW on average, which is 1.03% of the rated power of the wind turbine.

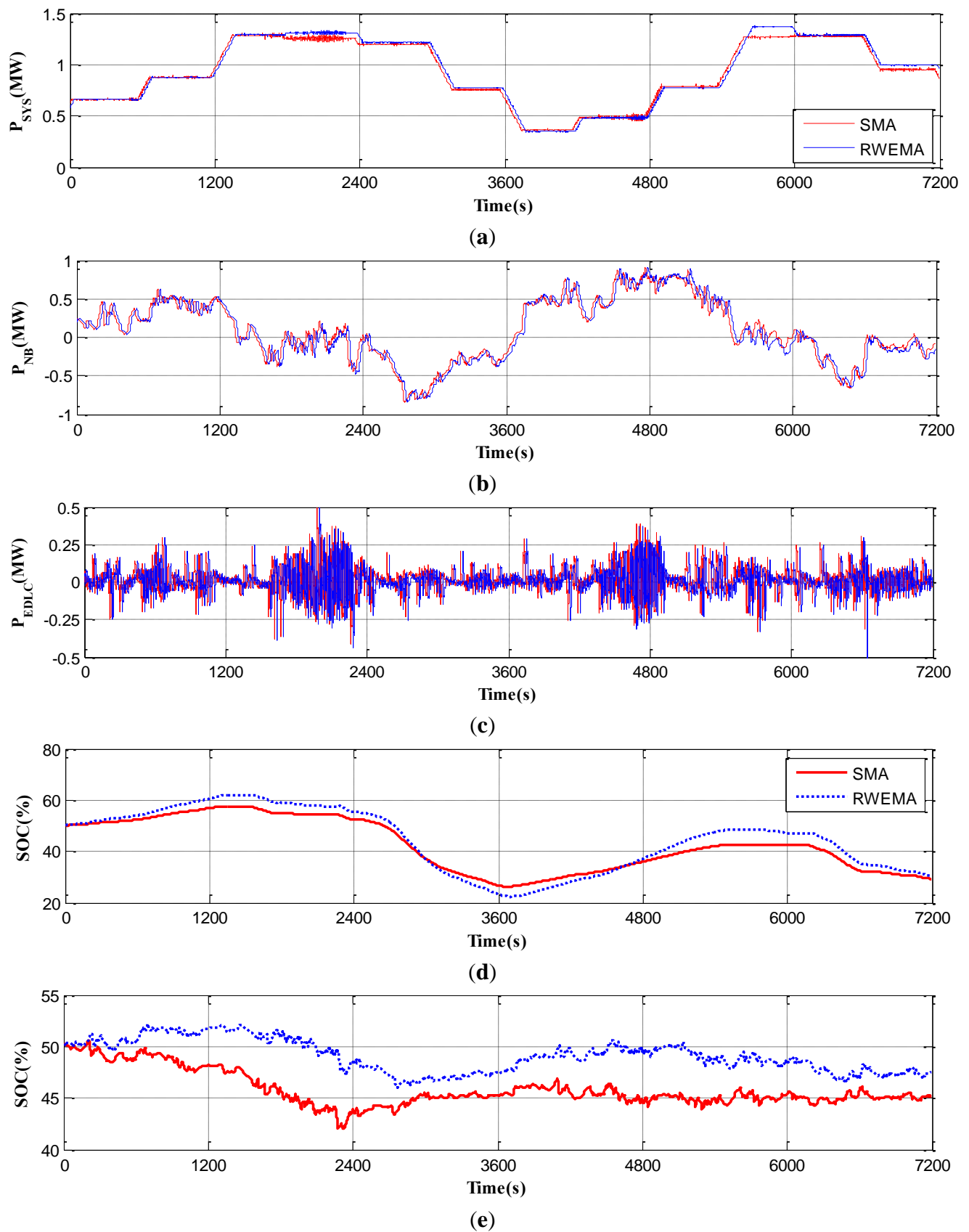
Table 4. Comparison between SMA and RWEMA for Cases 2 and 3. *BHI*: battery health index.

Case	Methods	P_{NB}^{\max} (MW)	<i>BHI</i>	$P_{NB, loss}^{\text{avg}}$ (kW)	$P_{EDLC, loss}^{\text{avg}}$ (kW)	$P_{\text{sys}}^{\text{avg}}$ (MW)
Case 2: Wind Pattern 1	SMA	0.924	13.94	137.57	14.52	0.938
	RWEMA	0.852	9.87	111.89	8.69	0.955
Case 2: Wind Pattern 2	SMA	0.912	13.25	121.51	17.09	0.929
	RWEMA	0.910	12.63	112.78	10.35	0.943
Case 3: $SOC_0 = 30\%$	SMA	0.919	17.79	165.82	15.35	0.881
	RWEMA	0.912	14.08	135.01	9.91	0.905
Case 3: $SOC_0 = 50\%$	SMA	0.921	16.72	144.31	15.39	0.926
	RWEMA	0.913	12.76	118.37	9.95	0.944
Case 3: $SOC_0 = 60\%$	SMA	0.920	15.77	135.92	15.33	0.944
	RWEMA	0.913	13.95	114.61	9.95	0.959

The simulation results for the Wind Pattern 2 also proved superiority of RWEMA over SMA as shown in Figure 12 although the differences in performance indices were not as large as those of Wind Pattern 1.

As shown in Figures 11b and 12b, the status of charge/discharge of NB changes frequently and the magnitude of energy absorption and release is not regular in this Wind-HESS application. Therefore, the cycle life of NB may be decreased. Basically, achievable cycle count (ACC) of a battery is increased when the depth of discharge (DOD) is decreased [24,25]. However, the actual cycle life of a battery should be evaluated by the amount of transferred energy during its whole life rather than the cycle count [24]. Since the DOD of NB in this application depends on the wind regime, it is hard to estimate the exact cycle life. Therefore, we approximately estimate the cycle life of the NB based on the average DOD. From our simulation, the average DOD per charge/discharge cycle was about 0.3. Based on the result of [24], the total transferrable energy with DOD = 0.3 is about 82% of that with DOD = 1.0. In other words, the cycle life of the NB in this application is decreased by 18% comparing to the full-charge-discharge application. Considering that the full-charge-discharge is an ideal case, it is thought that the cycle life degradation in this application is not severe in practice.

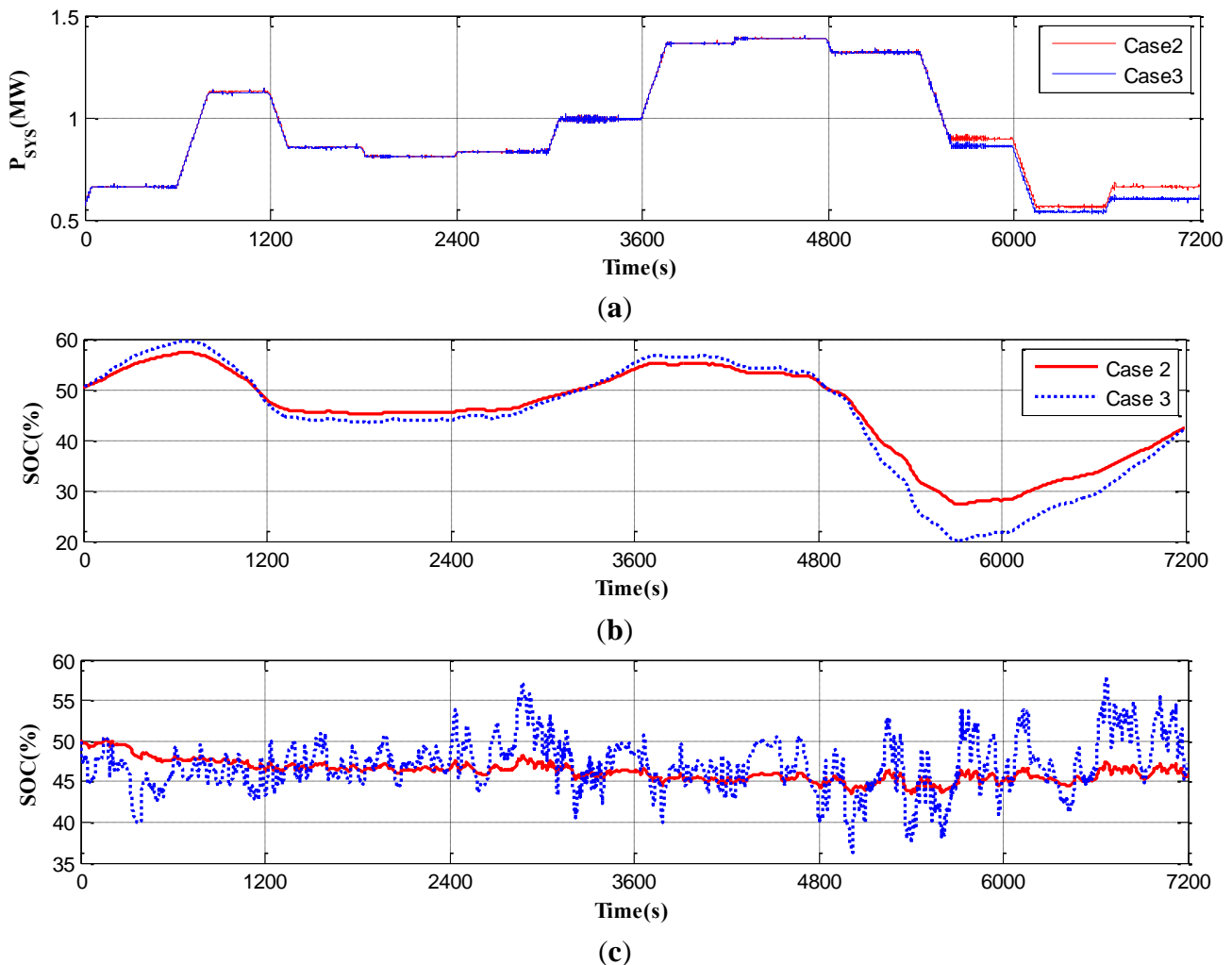
Figure 12. Simulation results for Case 2 with Wind Pattern 2: (a) total power output; (b) NB power output; (c) EDLC power output; (d) SOC level of NB; and (e) SOC level of EDLC.



4.4. Case 3: Reduced Hybrid Energy Storage System Capacity

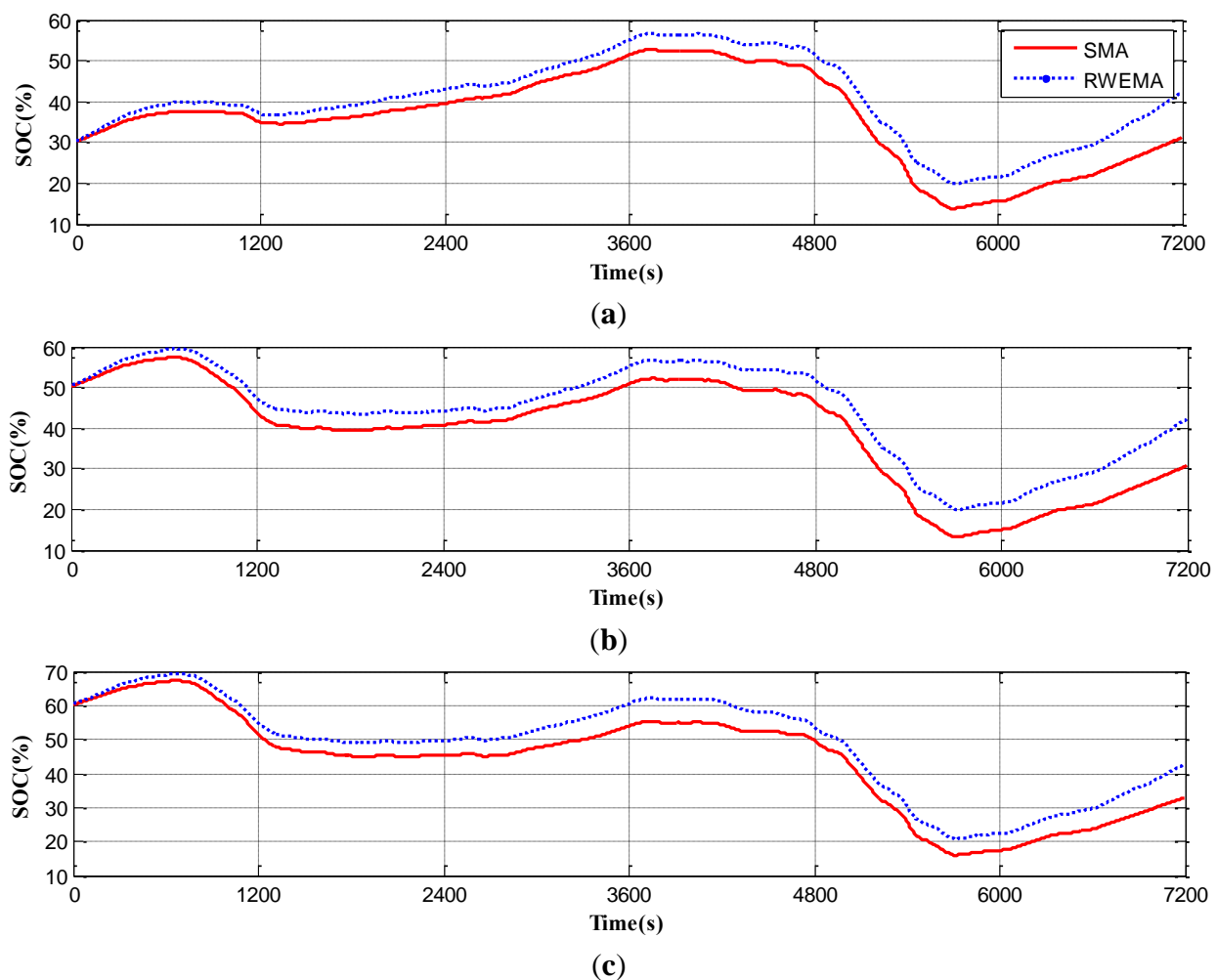
In this case, in order to verify the effect of capacity size on the proposed algorithm performance, HESS with a lower capacity was used. The capacity of the EDLC was set to 0.0043 MW h, which is about 20% of Case 2. For the capacity of NB, we found the minimum value at which the *SOC* level could be kept within the safe operating limits. With the proposed RWEMA, the value was 0.231 MW h, which is about 75% of that of Case 2. Figure 13 compares the simulation results of Cases 2 and 3 for the Wind Pattern 1. As shown in Figure 13a, the system outputs of the two cases were the same before 4800 s, since the *SOC*s of NB for both cases were maintained between 40% and 60%. After 4800 s, the system output was reduced somewhat in Case 3 since more energy was charged to NB. It can be also observed that the *SOC* level of NB and EDLC in Case 3 vary more than that in Case 2, due to the reduced capacity. As summarized in the Rows 2 and 5 of Table 4, power losses of NB and EDLC in Case 3 were increased by 5.8% and 14.5%, respectively. *BHI* was increased by 29.3% while the total system power output was decreased by 1.15%. Although the performance is degraded with reduced HESS capacity, the proposed RWEMA and *SOC* control strategy successfully managed the *SOC* level of NB and EDLC.

Figure 13. Comparison between the results of Cases 2 and 3 with Wind Pattern 1 and $SOC_0 = 50\%$: (a) total power output; (b) *SOC* level of NB; and (c) *SOC* level of EDLC.



We also compared the performance of the SMA method and RWEMA. We conducted the simulations for three different initial SOC levels (30%, 50%, and 60%), while all the other settings are the same. In this case, we assumed that the NB and EDLC will keep operating, even if the SOC level is outside the safe operating limits. As shown in Figure 14, RWEMA could successfully maintain the SOC level of NB within the required limit in all three simulations, whereas the SMA failed to meet the requirement. The minimum NB capacity required to maintain the SOC level within the operating limits with the SMA method was 0.305 MW h, which is 24.32% larger than that with RWEMA. Therefore, the proposed method can lower the storage capacity requirement of the HESS. The performance indices summarized in Table 4 also support the superiority of the RWEMA over the SMA method. The maximum absolute power of NB was almost the same in the two methods, but the *BHI* was reduced by 18.87% on average. The power losses of NB and EDLC decreased by 17.50% and 35.29%, respectively, and the total system power output was increased by 0.19 MW on average.

Figure 14. SOC level of NB with different initial values: (a) initial SOC = 30%; (b) initial SOC = 50%; and (c) initial SOC = 60%.



4.5. Case 4: Effect of Tuning Constant

In order to evaluate the impact of the tuning constant on system performance, we performed three simulation cases with different tuning constant sets of NB as depicted in Table 5. Set 1 is the

reference case; the gap between the consecutive tuning constants was doubled in Set 2, while the gap was halved in Set 3. The other simulation settings, including the tuning constant of EDLC, were kept the same as those in Case 3.

Table 5. NB tuning constant sets used in Case 4.

Battery SOC Level	Tuning constant (α_{NB})		
	Set 1	Set 2	Set 3
$75\% \leq SOC_{NB}$	1.25	1.55	1.10
$70\% \leq SOC_{NB} < 75\%$	1.15	1.35	1.05
$60\% \leq SOC_{NB} < 70\%$	1.05	1.15	1.00
$40\% \leq SOC_{NB} < 60\%$	1.00	1.00	1.00
$35\% \leq SOC_{NB} < 40\%$	0.85	0.75	0.90
$30\% \leq SOC_{NB} < 35\%$	0.75	0.55	0.85
$SOC_{NB} < 30\%$	0.65	0.35	0.80

The results are shown in Figure 15 and the performance indices are summarized in Table 6. The maximum absolute power of NB and the loss of HESS were the smallest in Case 3, while the *BHI* was the smallest in Case 2. As shown in Figure 15a, the system power output and the *SOC* profile were almost the same for three simulation cases before 5600 s. Subsequently, the system output reference was the lowest in the result with Set 2, since the tuning constant of Set 2 is the smallest for low *SOC* levels. Therefore, the magnitude of charging power would be the maximum in the results with Set 2. As a result, the power loss of NB was the most increased. On the other hand, the recovery of the *SOC* level with Set 3 was the slowest. Furthermore, in the simulation with Set 3, the *SOC* level was less than the low operating limit, as shown in Figure 15b. Therefore, the value of the tuning constant should be selected carefully considering the tradeoff between the loss and the effectiveness of the NB usage.

Figure 15. Simulation results for Case 4 with different tuning constant sets: (a) total system power output; and (b) *SOC* level of NB.

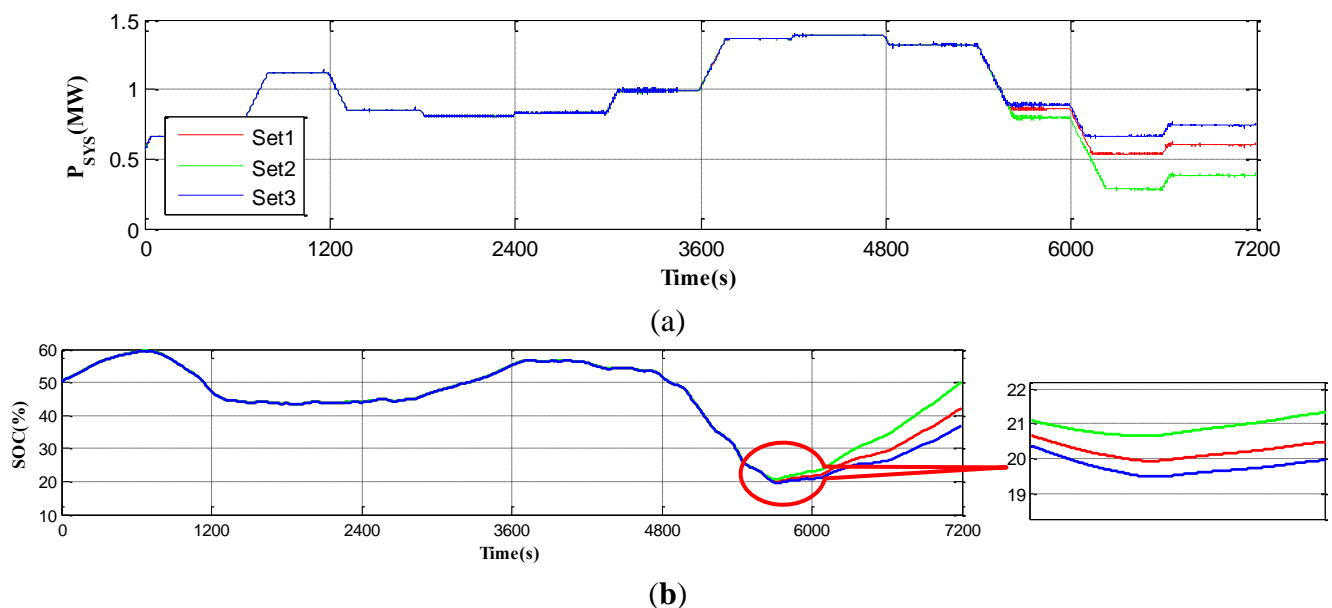


Table 6. Impact of tuning constant to system performance.

Tuning constant set	P_{NB}^{max} (MW)	BHI	$P_{NB, loss}^{avg}$ (kW)	P_{sys}^{avg} (MW)
Set 1	0.913	12.76	118.37	0.944
Set 2	0.997	11.75	147.29	0.906
Set 3	0.799	13.51	102.04	0.967

5. Conclusions

This paper proposed a novel RWEMA of a wind-HESS system to denoise and flatten the wind power output. A real-time DWT was used to decompose the 1-s sampled wind power output into high-frequency and low-frequency components. The high-frequency components were used as a reference of the EDLC, while the low-frequency terms were used to calculate the reference of the NB. SOC control strategies of EDLC and NB were also proposed by using the tuning constant concept. In addition, 1-min and 10-min RRL requirements can be met by the proposed RWEMA.

The simulation models of the NB and EDLC energy storage system were developed in the RTDS/RSCAD software. A configuration interface was also developed to modify the simulation parameters of the model. The proposed RWEMA has been tested in real-time by using the RTDS hardware and software. The simulation results demonstrated the effectiveness of the proposed control algorithm in denoising and flattening wind power output, and managing the SOC level of storage. The results also showed that the required capacity ratings of storage used in RWEMA were smaller than those of the conventional SMA-based technique. Since the proposed approach uses a simple DWT-based structure without any prediction technique, it can be easily implemented in real-time applications. In order to move beyond the simulation level and into the hardware implementation, many practical issues and requirements still need to be considered, such as data acquisition, communication media and protocol, data management, and selection of processor. The proposed method will be implemented as an actual hardware controller and be tested with the real Wind-HESS system in the future.

Acknowledgments

This work was partially supported by Korea Institute of Energy Technology Evaluation and Planning (KETEP) grant funded by Korea Government Ministry of Trade, Industry and Energy (No. 20123010020080). This work was also partially supported by the National Research Foundation of Korea (NRF) grant funded by the Korea Government (MSIP) (No. 2010-0028509).

Author Contributions

Tran Thai Trung developed the simulation models and wrote the first draft of the paper. Tran Thai Trung and Seok-II Go completed the simulation. Joon-Ho Choi and Soon-Ryul Nam discussed the results and implications, and commented on the manuscript. Seon-Ju Ahn coordinated the main theme of this paper, and thoroughly reviewed and edited the manuscript. All the authors read and approved the final manuscript.

Conflicts of Interest

The authors declare no conflict of interest.

References

1. Fox, B. Introduction. In *Wind Power Integration: Connection and System Operational Aspects*; The Institution of Engineering and Technology (IET): London, UK, 2007; pp. 14–18.
2. Zhang, J.; Cheng, M.; Chen, Z.; Fu, X. Pitch angle control for variable speed wind turbines. In *Proceedings of the Third International Conference on Electric Utility Deregulation and Restructuring and Power Technologies, DRPT 2008*, Nanjing, China, 6–9 April 2008; pp. 2691–2696.
3. Abedini, A.; Nasiri, A. Output power smoothing for wind turbine permanent magnet synchronous generators using rotor inertia. *Electr. Power Compon. Syst.* **2008**, *37*, 1–19.
4. Barton, J.P.; Infield, D.G. Energy storage and its use with intermittent renewable energy. *IEEE Trans. Energy Convers.* **2004**, *19*, 441–448.
5. Abbey, C.; Joos, G. Supercapacitor energy storage for wind energy applications. *IEEE Trans. Ind. Appl.* **2007**, *43*, 769–776.
6. Ushiwata, K.; Shishido, S.; Takahashi, R.; Murata, T.; Tamura, J. Smoothing control of wind generator output fluctuation by using electric double layer capacitor. In *Proceedings of the International Conference on Electrical Machines and Systems (ICEMS)*, Seoul, Korea, 8–11 October 2007; pp. 308–313.
7. Tanabe, T.; Sato, T.; Tanikawa, R.; Aoki, I.; Funabashi, T.; Yokoyama, R. Generation scheduling for wind power generation by storage battery system and meteorological forecast. In *Proceedings of the 2008 IEEE Power and Energy Society General Meeting—Conversion and Delivery of Electrical Energy in the 21st Century*, Pittsburgh, PA, USA, 20–24 July 2008; pp. 1–7.
8. Sheikh, M.R.I.; Mueen, S.M.; Takahashi, R.; Murata, T.; Tamura, J. Minimization of fluctuations of output power and terminal voltage of wind generator by using STATCOM/SMES. In *Proceedings of the 2009 IEEE Bucharest PowerTech*, Bucharest, Romania, 28 June–2 July 2009; pp. 1–6.
9. Yoshimoto, K.; Nanahara, T.; Koshimizu, G. New control method for regulating state-of-charge of a battery in hybrid wind power/battery energy storage system. In *Proceedings of the 2006 IEEE PES Power Systems Conference and Exposition, PSCE '06*, Atlanta, GA, USA, 29 October–1 November 2006; pp. 1244–1251.
10. Li, W.; Joós, G.; Bédanger, J. Real-time simulation of a wind turbine generator coupled with a battery supercapacitor energy storage system. *IEEE Trans. Ind. Electron.* **2010**, *57*, 1137–1145.
11. Suvire, G.O.; Mercado, P. Active power control of a flywheel energy storage system for wind energy applications. *IET Renew. Power Gener.* **2012**, *6*, 9–16.
12. Mishra, Y.; Mishra, S.; Li, F. Coordinated tuning of DFIG-based wind turbines and batteries using bacteria foraging technique for maintaining constant grid power output. *IEEE Syst. J.* **2012**, *6*, 16–26.
13. Li, X.; Li, Y.; Han, X.; Hui, D. Application of fuzzy wavelet transform to smooth wind/PV hybrid power system output with battery energy storage system. *Energy Procedia* **2011**, *12*, 994–1001.

14. Jiang, Q.; Hong, H. Wavelet-based capacity configuration and coordinated control of hybrid energy storage system for smoothing out wind power fluctuations. *IEEE Trans. Power Syst.* **2013**, *28*, 1363–1372.
15. Xia, R.; Meng, K.; Qian, F.; Wang, Z.-L. Online wavelet denoising via a moving window. *Acta Autom. Sin.* **2007**, *33*, 897–901.
16. RTDS Technologies. Power System Simulator Hardware. Available online: <http://rtds.com/hardware/hardware.html> (accessed on 30 May 2014).
17. Omar, N.; Daowd, M.; Hegazy, O.; Bossche, P.V.D.; Coosemans, T.; Mierlo, J.V. Electrical double-layer capacitors in hybrid topologies—Assessment and evaluation of their performance. *Energies* **2012**, *5*, 4533–4568.
18. Oldham, K.B. A Gouy-Chapman-Stern model of the double layer at a (metal)/(ionic liquid) interface. *J. Electroanal. Chem.* **2008**, *613*, 131–138.
19. MathWorks. Implement Generic Supercapacitor Model—Simulink. Available online: <http://www.mathworks.com/help/physmod/sps/powersys/ref/supercapacitor.html> (accessed on 3 June 2014).
20. Tremblay, O.; Dessaint, L.-A.; Dekkiche, A.-I. A generic battery model for the dynamic simulation of hybrid electric vehicles. In Proceedings of the IEEE Vehicle Power and Propulsion Conference, VPPC 2007, Arlington, TX, USA, 9–12 September 2007; pp. 284–289.
21. Gevorgian, V.; Booth, S. *Review of Prepa Technical Requirements for Interconnecting Wind and Solar Generation*; National Renewable Energy Laboratory: Golden, CO, USA, 2013.
22. Fox, B. Operation of power systems. In *Wind Power Integration: Connection and System Operational Aspects*; The Institution of Engineering and Technology (IET): London, UK, 2007; pp. 160–170.
23. Chan, F.-P.; Fu, A.-C.; Yu, C. Haar wavelets for efficient similarity search of time-series: With and without time warping. *IEEE Trans. Knowl. Data Eng.* **2003**, *15*, 686–705.
24. Han, S.; Han, S. Economic feasibility of V2G frequency regulation in consideration of battery wear. *Energies* **2013**, *6*, 748–765.
25. Peterson, S.B.; Apt, J.; Whitacre, J. Lithium-ion battery cell degradation resulting from realistic vehicle and vehicle-to-grid utilization. *J. Power Sources* **2010**, *195*, 2385–2392.